An Infinite Series Solution for the Creeping Radial Entrance Flow of a Newtonian Fluid

Ajay Chatterjee
Dept. of Chemical Engineering, The Pennsylvania State University, University Park, PA 16802

The entrance flow of a Newtonian fluid through the idealized radial flow geometry in Figure 1 is of considerable theoretical interest in its own right (Bird et al., 1960). From a practical viewpoint, the geometry is useful since it idealizes the salient features of hydrostatic thrust bearings (Hunt and Torbe, 1962), injection molds (Middleman, 1977), and radial flow plasma reactors (Hollahan and Rosler, 1978). In this work we develop a semianalytical solution to this problem in the creeping flow limit. Previous works have focused on developing regular perturbation type of expansions from the fully developed base flow to calculate the effect of fluid inertia on the velocity field and the pressure distribution between the circular plates (Livesey, 1960; Moller, 1963; Peube, 1963; Jackson and Symmons, 1965a,b; Chen, 1966). Apart from the recent finite-difference calculation (Chatterjee and White, 1989), the only attempt at including entrance effects was made by Parmet and Saibel (1965), who developed an analytical solution in the low Reynolds number limit. Unfortunately, their solution is incorrect, since they assumed the applicability of an arbitrarily specified velocity distribution (in their case a vorticity-free velocity profile) at the plane $z=0$. To construct the solution we employ the now standard technique (Takematsu, 1966; Vrentas and Duda, 1967; Dagan et al., 1982) of first partitioning the flow field into two geometrically simpler regions: the flow field within the pipe and the flow region bounded by the circular plates, and then combining the solution valid in each region by imposing continuity requirements on the field variables and their first normal derivatives at the plane $z=0$. The present solution becomes computationally attractive as the aspect ratio ($\kappa = L/R$) increases.

Infinite Series Solutions

Pipe region $0 \le \xi \le 1$, $\eta \le 0$

The solution for the flow field in this region were given by Vrentas and Duda (1967), from which the expressions for the dimensionless stream function ψ, vorticity ω, axial velocity u, and radial velocity v are:

$$\psi(\xi,\eta)=\xi^2\left(1-\frac{\xi^2}{2}\right) - \sum_{n=1}^{\infty} N_n \xi J_1(\beta_n\xi)e^{\beta_n\eta} - \sum_{n=1}^{\infty}\frac{M_n}{2\beta_n}\xi J_1(\beta_n\xi)\eta e^{\beta_n\eta} + \sum_{n=1}^{\infty}\frac{2N_n\beta_n^2 J_0(\beta_n)}{\pi}\int_0^{\infty}\frac{\cos\rho\eta\, W(\xi,\rho)}{(\beta_n^2+\rho^2)\rho P(\rho)}d\rho - \sum_{n=1}^{\infty}\frac{M_n J_0(\beta_n)}{\pi}\int_0^{\infty}\frac{\cos\rho\eta\,(\beta_n^2-\rho^2)\,W(\xi,\rho)}{(\beta_n^2+\rho^2)^2\rho P(\rho)}d\rho \quad (1)$$

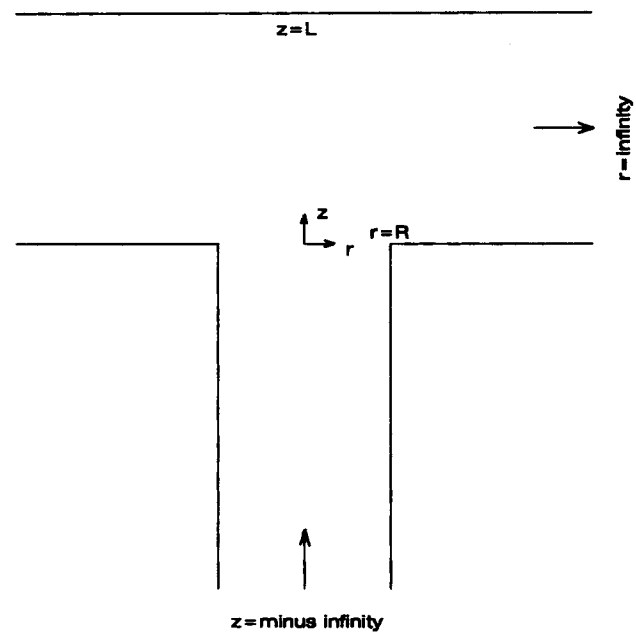

Figure 1. Idealized radial flow geometry and its coordinate system.

Present address of A. Chatterjee: Intel Corporation, Mail Stop RN2-40, 2200 Mission College Boulevard, P.O. Box 58119, Santa Clara, CA 95052.

$$\omega(\xi,\eta) = -4\xi - \sum_{n=1}^{\infty} M_n J_1(\beta_n\xi)e^{\beta_n\eta} + \sum_{n=1}^{\infty} \frac{4N_n\beta_n^2 J_0(\beta_n)}{\pi} \int_0^{\infty} \frac{\cos\rho\eta\, I_1(\rho\xi) I_1(\rho)}{(\beta_n^2+\rho^2)P(\rho)}\, d\rho - \sum_{n=1}^{\infty} \frac{2M_n J_0(\beta_n)}{\pi} \int_0^{\infty} \frac{\cos\rho\eta(\beta_n^2-\rho^2) I_1(\rho\xi) I_1(\rho)}{(\beta_n^2+\rho^2)^2 P(\rho)}\, d\rho \quad (2)$$

$$u(\xi,\eta) = 2(1-\xi^2) - \sum_{n=1}^{\infty} N_n\beta_n J_0(\beta_n\xi)e^{\beta_n\eta} - \sum_{n=1}^{\infty} \frac{M_n}{2} J_0(\beta_n\xi)\eta e^{\beta_n\eta} + \sum_{n=1}^{\infty} \frac{2N_n\beta_n^2 J_0(\beta_n)}{\pi} \int_0^{\infty} \frac{\cos\rho\eta\, S(\xi,\rho)}{(\beta_n^2+\rho^2)P(\rho)}\, d\rho - \sum_{n=1}^{\infty} \frac{M_n J_0(\beta_n)}{\pi} \int_0^{\infty} \frac{\cos\rho\eta\,(\beta_n^2-\rho^2) S(\xi,\rho)}{(\beta_n^2+\rho^2)^2 P(\rho)}\, d\rho \quad (3)$$

$$v(\xi,\eta) = \sum_{n=1}^{\infty} N_n\beta_n J_1(\beta_n\xi)e^{\beta_n\eta} + \sum_{n=1}^{\infty} \frac{M_n}{2} J_1(\beta_n\xi)\eta e^{\beta_n\eta} + \sum_{n=1}^{\infty} \frac{M_n}{2\beta_n} J_1(\beta_n\xi)e^{\beta_n\eta} + \sum_{n=1}^{\infty} \frac{2N_n\beta_n^2 J_0(\beta_n)}{\pi} \int_0^{\infty} \frac{\sin\rho\eta\, W(\xi,\rho)}{(\beta_n^2+\rho^2)P(\rho)}\, d\rho - \sum_{n=1}^{\infty} \frac{M_n J_0(\beta_n)}{\pi} \int_0^{\infty} \frac{\sin\rho\eta\,(\beta_n^2-\rho^2) W(\xi,\rho)}{(\beta_n^2+\rho^2)^2 P(\rho)}\, d\rho \quad (4)$$

The quantities $P(\rho)$, $S(\xi,\rho)$, and $W(\xi,\rho)$ are given by:

$$P(\rho) = I_1^2(\rho) - I_0(\rho)I_2(\rho)$$
$$S(\xi,\rho) = \xi I_1(\rho\xi)I_1(\rho) - I_0(\rho\xi)I_2(\rho)$$
$$W(\xi,\rho) = \xi^2 I_2(\rho\xi)I_1(\rho) - \xi I_1(\rho\xi)I_2(\rho) \quad (5, 6, 7)$$

Matching plane $\eta = \hat{\eta} = 0$

The coordinate surface $\eta = \hat{\eta} = 0$ represents the matching plane at which the dimensionless axial and radial velocity components are prescribed in a general way by using Fourier-Bessel series. Thus, for $0 \le \xi \le 1$, we write:

$$u^*(\xi) = \sum_{n=1}^{\infty} A_n J_0(\alpha_n\xi) \quad v^*(\xi) = \sum_{n=1}^{\infty} B_n J_1(\beta_n\xi) \quad (8, 9)$$

Radial flow region $0 \le \hat{\eta} \le 1$, $\xi \ge 0$

The general expression for the dimensionless stream function field in the radial flow region was given by Parmet and Saibel (1965) in the form:

$$\hat{\psi}(\xi,\hat{\eta}) = \int_0^{\infty} \xi J_1(\beta\xi)[A(\beta)\cosh\kappa\beta\hat{\eta} + B(\beta)\sinh\kappa\beta\hat{\eta}]d\beta + \hat{\eta}\int_0^{\infty} \xi J_1(\beta\xi)[C(\beta)\cosh\kappa\beta\hat{\eta} + D(\beta)\sinh\kappa\beta\hat{\eta}]d\beta \quad (10)$$

As shown by Parmet and Saibel (1965), expressions for the unknown functions $A(\beta)$, $B(\beta)$, $C(\beta)$, and $D(\beta)$ can be obtained by imposing boundary conditions on the stream function field and then using the properties of the Hankel transform. The procedure yields:

$$A(\beta) = \int_0^1 \xi u^*(\xi) J_0(\beta\xi)d\xi = \sum_{n=1}^{\infty} \frac{A_n\alpha_n J_1(\alpha_n) J_0(\beta)}{\alpha_n^2 - \beta^2} \quad (11)$$

$$B(\beta) = -\frac{A(\beta)[\kappa\beta + \sinh\kappa\beta\cosh\kappa\beta]}{\sinh^2\kappa\beta - \kappa^2\beta^2} - \frac{\kappa^2\beta^2 E(\beta)}{\sinh^2\kappa\beta - \kappa^2\beta^2} \quad (12)$$

$$C(\beta) = \frac{\kappa\beta A(\beta)[\kappa\beta + \sinh^2\kappa\beta\cosh\kappa\beta]}{\sinh^2\kappa\beta - \kappa^2\beta^2} + \frac{\kappa\beta E(\beta)\sinh 6\kappa\beta}{\sinh^2\kappa\beta - \kappa^2\beta^2} \quad (13)$$

$$D(\beta) = -\frac{\kappa\beta A(\beta)\sinh^2\kappa\beta}{\sinh^2\kappa\beta - \kappa^2\beta^2} + \frac{\kappa\beta E(\beta)[\kappa\beta - \sinh\kappa\beta\cosh\kappa\beta]}{\sinh^2\kappa\beta - \kappa^2\beta^2} \quad (14)$$

where

$$E(\beta) = -\int_0^1 \xi v^*(\xi) J_1(\beta\xi)d\xi = \sum_{n=1}^{\infty} \frac{B_n\beta_n J_0(\beta_n) J_1(\beta)}{\beta_n^2 - \beta^2} \quad (15)$$

This specifies completely the solution for the radial flow region in terms of the velocity components at the matching plane $\eta = \hat{\eta} = 0$. To compute unique values of the four sets of unknown coefficients A_n, B_n, M_n, and N_n, it is necessary now to impose matching conditions.

Matching Equations

A full set of four matching equations can be derived by noting first that the solution valid within the pipe (Eqs. 3 and 4) has to match kinematically with the velocity components at the plane $\eta = \hat{\eta} = 0$ given by the Fourier-Bessel series in Eqs. 8 and 9, and second, by requiring that the vorticity and its first axial derivative (Vrentas and Duda, 1967), or equivalently the stress fields (Dagan et al., 1982) be continuous at the matching plane. The following four matching equations can be obtained by imposing the constraints described above:

$$\frac{1}{2}A_k J_1(\alpha_k) = \frac{8}{\alpha_k^3} + \sum_{n=1}^{\infty} \frac{N_n\beta_n J_0(\beta_n)}{\beta_n^2 - \alpha_k^2}\alpha_k + \sum_{n=1}^{\infty} \frac{2N_n\beta_n^2 J_0(\beta_n)}{\pi} \int_0^{\infty} \frac{1}{(\beta_n^2+\rho^2)} \left[\frac{\alpha_k[I_1^2(\rho) - I_0^2(\rho)]}{(\rho^2+\alpha_k^2)P(\rho)} + \frac{2\alpha_k^3 I_0(\rho)I_1(\rho)}{\rho(\rho^2+\alpha_k^2)^2 P(\rho)} \right] d\rho - \sum_{n=1}^{\infty} \frac{M_n J_0(\beta_n)}{\pi} \int_0^{\infty} \frac{(\beta_n^2-\rho^2)}{(\beta_n^2+\rho^2)^2} \left[\frac{\alpha_k[I_1^2(\rho) - I_0^2(\rho)]}{(\rho^2+\alpha_k^2)P(\rho)} + \frac{2\alpha_k^3 I_0(\rho)I_1(\rho)}{\rho(\rho^2+\alpha_k^2)^2 P(\rho)} \right] d\rho \quad (16)$$

$$B_k = N_k\beta_k + \frac{M_k}{2\beta_k} \quad (17)$$

$$\frac{2}{\kappa}\sum_{n=1}^{\infty} A_n\alpha_n J_1(\alpha_n)$$

$$\times\int_0^{\infty}\frac{\kappa\beta^2}{(\beta^2-\alpha_n^2)(\beta^2-\beta_k^2)}\frac{\sinh^2\kappa\beta}{\sinh^2\kappa\beta-\kappa^2\beta^2}J_0(\beta)J_1(\beta)\,d\beta$$

$$-\frac{2}{\kappa}\sum_{n=1}^{\infty} B_n\beta_n J_0(\beta_n)$$

$$\times\int_0^{\infty}\frac{\kappa\beta^2}{(\beta^2-\beta_n^2)(\beta^2-\beta_k^2)}\left[\frac{\kappa\beta-\sinh\kappa\beta\cosh\kappa\beta}{\sinh^2\kappa\beta-\kappa^2\beta^2}\right]J_1^2(\beta)d\beta$$

$$=\frac{4}{\beta_k^2}-\frac{1}{2}\frac{M_kJ_0(\beta_k)}{\beta_k}$$

$$-\sum_{n=1}^{\infty}\frac{4N_n\beta_n^2J_0(\beta_n)}{\pi}\int_0^{\infty}\frac{I_1^2(\rho)}{(\beta_n^2+\rho^2)(\beta_k^2+\rho^2)P(\rho)}d\rho$$

$$+\sum_{n=1}^{\infty}\frac{2M_nJ_0(\beta_n)}{\pi}\int_0^{\infty}\frac{(\beta_n^2-\rho^2)I_1^2(\rho)}{(\beta_n^2+\rho^2)^2(\beta_k^2+\rho^2)P(\rho)}d\rho \qquad (18)$$

$$2\sum_{n=1}^{\infty} A_n\alpha_n J_1(\alpha_n)\int_0^{\infty}\frac{\kappa\beta^3}{(\alpha_n^2-\beta^2)(\beta^2-\beta_k^2)}$$

$$\times\left[\frac{\kappa\beta+\sinh\kappa\beta\cosh\kappa\beta}{\sinh^2\kappa\beta-\kappa^2\beta^2}\right]J_0(\beta)J_1(\beta)\,d\beta$$

$$-2\sum_{n=1}^{\infty} B_n\beta_n J_0(\beta_n)$$

$$\times\int_0^{\infty}\frac{\kappa\beta^3}{(\beta^2-\beta_n^2)(\beta^2-\beta_k^2)}\frac{\sinh^2\kappa\beta}{\sinh^2\kappa\beta-\kappa^2\beta^2}J_1^2(\beta)\,d\beta$$

$$=-\frac{1}{2}\kappa M_kJ_0(\beta_k) \qquad (19)$$

The existence of the improper integrals occurring in the matching equations may easily be proved by first utilizing the asymptotic expansions of the Bessel functions to show that the integrands are bounded on the real line and then demonstrating that the integrals are smaller in absolute value than certain well defined improper integrals. For the numerical computation of the first n coefficients A_n, B_n, M_n, and N_n, the four matching equations may be consolidated into a matrix equation, successively larger truncations of which can be solved to yield accurate values of these unknown coefficients. Truncation after n terms requires the solution of $4n$ linear algebraic equations in $4n$ unknowns. Calculation of the elements of the $4n \times 4n$ coefficient matrix takes up the bulk of the computation time, especially since the matrix has to be evaluated separately for each value of the aspect ratio. It, however, helps to note that three of the eight improper integrals involved in the computation of the matrix are symmetric in n and k. The integrals can all be calculated using standard IMSL algorithms (IMSL, 1989).

Results

Figure 2 depicts the dimensionless total flow rate computed from Eq. 8 as a function of the number of terms in each infinite series, the exact value being $Q=\pi$. The figure indicates that the rate of convergence deteriorates with diminishing aspect ratio. A similar conclusion is reached when the convergence behavior of the centerline axial velocity $u^*(0)$ is investigated, $u^*(0)$ being given by the sum of the first n coefficients A_n. Figure 3 shows the absolute error between the nth partial sum

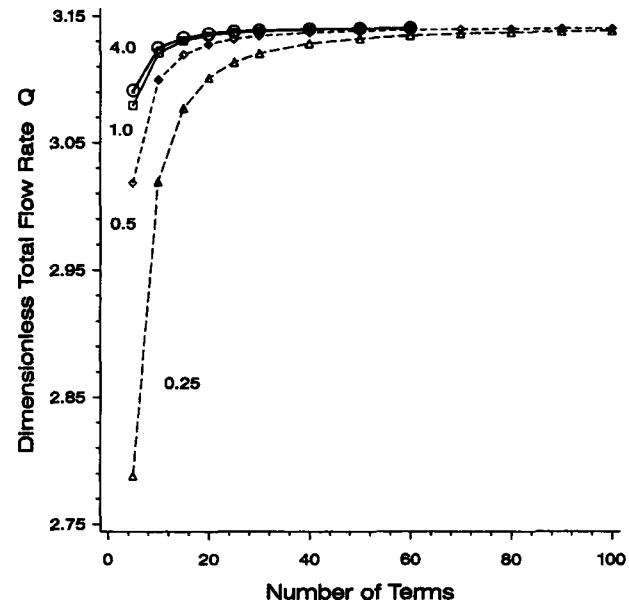

Figure 2. Convergence test for the dimensionless total flow rate Q as a function of the number of terms in each infinite series for aspect ratios of 1/4, 1/2, 1, 2, and 4.

The curves for aspect ratios of 2 and 4 virtually are indistinguishable.

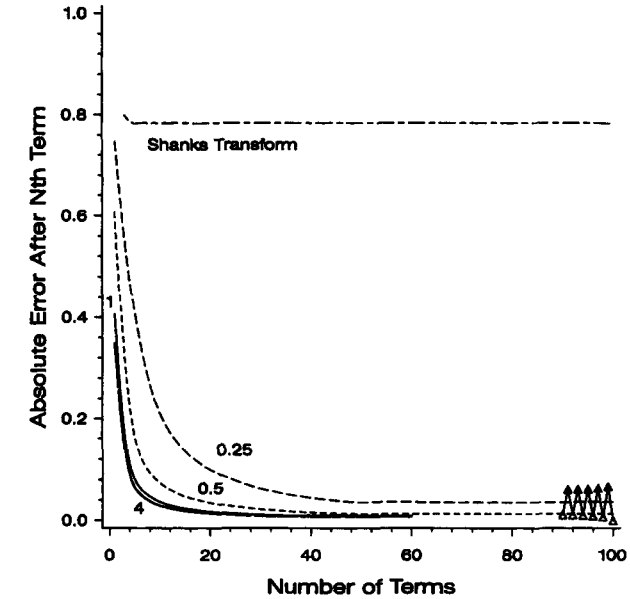

Figure 3. Absolute error between the nth partial sum in the expansion for the centerline axial velocity $u^*(0)$ and its final value for aspect ratios of 1/4, 1/2, 1, 2, and 4.

The curves for aspect ratios of 2 and 4 virtually are indistinguishable. The curve labeled "Shanks Transform" represents $u^*(0)$ for $\kappa = 1/4$ obtained after one application of Shanks nonlinear transform to the sequence of partial sums.

and the final value that was calculated using 60 terms for values of $\kappa \geq 1$ and 100 terms for $\kappa < 1$. This figure also indicates that oscillations in $u^*(0)$ have not completely damped out after 100 terms when $\kappa = 1/4$ (open triangles). Given this convergence behavior, for the computation of all subsequent results up to 100 terms were used for aspect ratios less than unity, whereas a maximum of 60 terms was deemed adequate for aspect ratios equal to or greater than unity. We mention, however, that the convergence behavior may be improved significantly by resorting to a nonlinear transformation due to Shanks (1955). In fact, a single application of this transformation provides a sequence that is invariant in the first three significant digits after only a few terms. Figure 3, "Shanks Transform," depicts $u^*(0)$ for an aspect ratio of $\kappa = 1/4$ after one application of the transform. In what follows we focus our discussion on some new results for the pressure and stress fields in the radial flow region. We point out, however, that for the range of aspect ratios studied, velocity profiles at the planes $z = 0$ and $r = R$ calculated using the infinite series show excellent agreement with the finite-difference results presented in the earlier article, the only exception being the velocity profile at an aspect ratio of $\kappa = 1/4$ at the plane $z = 0$. Furthermore, in the large aspect ratio limit (practically speaking beyond 2.0), the present calculations reproduce correctly the axial and radial velocity profiles at the plane $z = 0$ computed by Dagan et al. (1982) for the creeping flow through a finite orifice into an infinite half space. For brevity, we do not present these comparisons here.

Figures 4 and 5 display the dimensionless shear stress distributions (made dimensionless with $\mu Q/\pi R^3$, here Q denotes the dimensional total flow rate) on the surfaces of the circular plates at $z = 0, L$. These stress distributions are of considerable practical importance and may be calculated simply by evaluating the dimensionless vorticity at these surfaces from Eq. 10. The sharp corner $z = 0$, $r = R$, has been omitted from the calculation on the bottom plate surface, since the vorticity is singular at this point. The stress values for different aspect ratios have been normalized by multiplying them by κ^{-2}, since the fully developed shear stress profile scales as κ^2. At small aspect ratios, the flow changes quickly from axial to radial flow, and so the shear stress on the top plate at $z = L$ increases sharply from a value of zero at $r = 0$ to approximately its fully developed value at about $r = R$, as seen in Figure 5. However, as the aspect ratio increases beyond unity radial flow development occurs gradually, and so the shear stress at $z = L$ increases more slowly. We also note that on both the top and the bottom plates, for small aspect ratios the shear stress profiles rapidly assume the fully developed configuration, which has $1/r$ behavior, whereas for aspect ratios greater than unity entrance effects persist for a distance of a few pipe radii downstream of the entrance region. This happens because while the eigenfunctions describing the flow in this region decay on the scale of L, the radial coordinate is measured in terms of R, so that as $\kappa\ (= L/R)$ increases the eigenfunctions decay to the fully developed configuration over a longer radial length scale. Thus, in creeping flow the entrance length for this geometry goes as $0(L)$ and not $0(R)$. Figure 5 also indicates that as the aspect ratio increases beyond unity the maximum shear stress on the surface of the top plate at $z = L$ decreases in magnitude and it occurs further downstream of the entrance region.

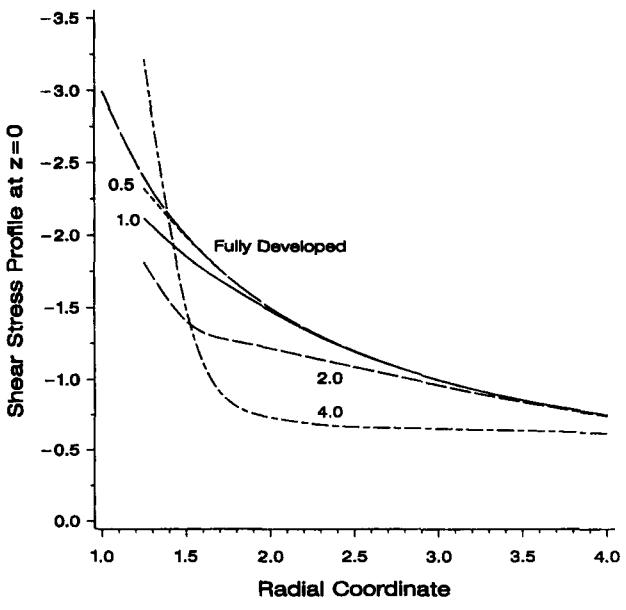

Figure 4. Comparison between the dimensionless shear stress profiles on the surface of the bottom circular plate at $z = 0$ for aspect ratios of 1/4, 1/2, 1, 2, and 4, and the fully developed profile.

The profiles for aspect ratios of 1/4 and 1/2 virtually are indistinguishable.

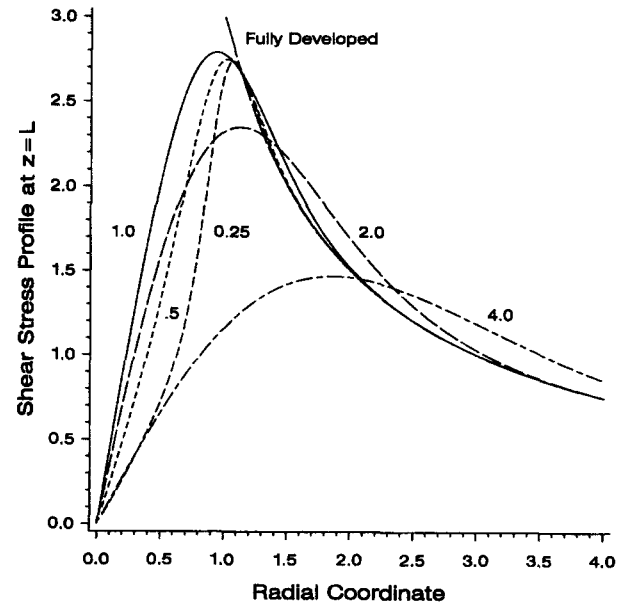

Figure 5. Comparison between the dimensionless shear stress profiles on the surface of the top circular plate at $z = L$ for aspect ratios of 1/4, 1/2, 1, 2 and 4, and the fully developed profile.

The normal component of the deviatoric stress tensor vanishes at the solid surfaces $z = 0, L$. The pressure distributions on these surfaces are also of practical interest and they may be computed directly by integrating the equation:

$$\frac{\partial \bar{P}}{\partial \xi} = -\frac{1}{\kappa \xi} \frac{\partial (\xi \hat{\omega})}{\partial \hat{\eta}} \tag{20}$$

The dimensionless pressure profiles at $z=0$, L depicted in Figures 6 and 7 for various aspect ratios were calculated by integrating the above equation from r to $r/R=10$, at which point the flow is fully developed and so the pressure is independent of the axial coordinate. The calculated pressure profiles, which have been made dimensionless with $\mu Q/\pi R^3$, have all been normalized by multiplying them with κ^3 since the fully developed profile, which displays an $\ln(R/r)$ behavior, scales as κ^{-3}. Once again, we note that entrance effects dissipate very quickly for low aspect ratios, but they persist for some distance downstream of the entrance region as the aspect ratio is increased beyond unity. We also observe that on the bottom plate surface the pressure exhibits a singularity at the sharp corner $r=R$, $z=0$, a point remarked by Dagan et al. (1982).

Table 1 presents a computation of the dimensionless total excess pressure drop (ΔP_E) for this entrance geometry as a function of the aspect ratio. The total excess pressure drop being defined here as the pressure drop due to entrance effects alone, that is, the pressure drop in addition to that due to Poiseuille flow in the pipe and fully developed flow in the radial flow region beyond $r=R$. As expected, the total excess pressure drop decreases with increasing aspect ratio, initially very sharply for small aspect ratios and then more gradually as the aspect ratio increases beyond unity and the influence of the top plate at $z=L$ is diminished. Since the excess pressure drop in the pipe is quite small (it is about 1% of the total excess pressure drop), the contribution to the total excess pressure drop comes mainly from the region $0\le z\le L$. The flow in this region may be viewed as (one half of) a modified Sampson flow (Sampson, 1891) with walls at $z=\pm L$. Consequently, since the effects of the wall at $z=L$ diminish with increasing aspect ratio, we expect the calculated total excess pressure drop to approach one half the pressure drop in a Sampson flow as

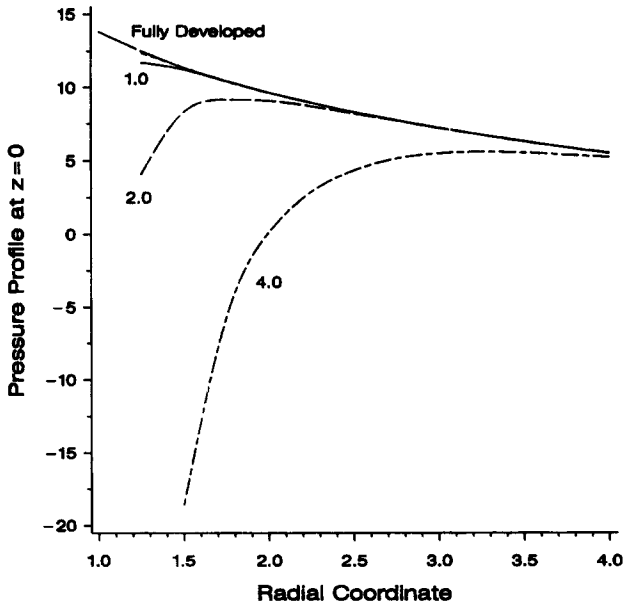

Figure 6. Comparison between the dimensionless pressure profiles on the surface of the bottom circular plate at $z=0$ for aspect ratios of 1/4, 1/2, 1, 2, and 4, and the fully developed profile.

The profiles for aspect ratios of 1/4 and 1/2 are not distinguishable from the fully developed profile.

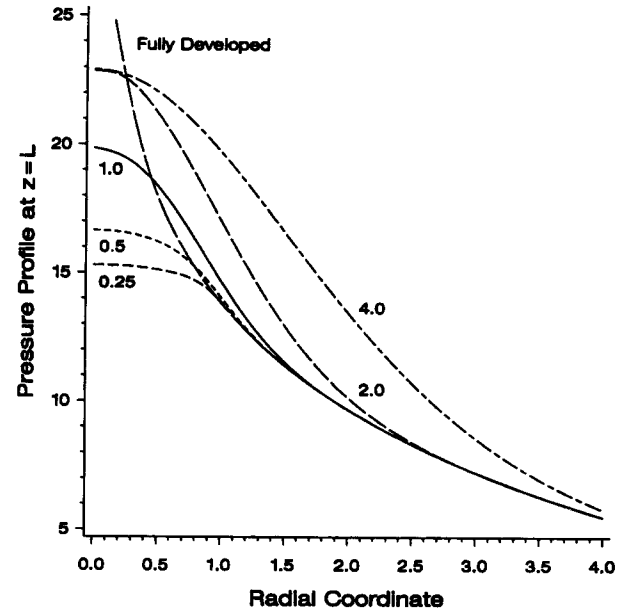

Figure 7. Comparison between the dimensionless pressure profiles on the surface of the top circular plate at $z=L$ for aspect ratios of 1/4, 1/2, 1, 2, and 4, and the fully developed profile.

the aspect ratio is increased. This is indeed what we find from Table 1. We observe that as the aspect ratio increases beyond unity, more precisely for $\kappa\ge 2$, the value of the computed total excess pressure drop is within a couple of percent of one half the value from Sampson's classic solution for Stokes flow through a hole in a plane wall, for which $1/2\Delta P=1.5\pi=4.712$.

The infinite series solution developed in this work converges rapidly and the solution appears to be most efficient for moderate to large aspect ratio geometries. Unless special transformation techniques are used to map the infinite flow field into a finite domain, with a finite-difference scheme the inflow and outflow boundaries must be set sufficiently far from the entrance region. The number of grid points required for a numerical solution thus increases with the entrance length. For the present geometry, the entrance length increases with the aspect ratio, while the infinite series converge rapidly for moderate to large aspect ratios; therefore, this solution may be particularly useful in moderate to large aspect ratio situations.

Notation

A_n, B_n, M_n, N_n = coefficients in the infinite series expansions

Table 1. Dimensionless Total Excess Pressure Drop (ΔP_E) as a Function of the Aspect Ratio (κ)

Aspect Ratio κ	Total Excess Pres. Drop ΔP_E
0.25	89.13
0.5	19.56
1.0	6.53
2.0	4.68
4.0	4.65

I_0, I_1, I_2 = modified Bessel functions of the first kind of order 0, 1, and 2, respectively
J_0, J_1 = ordinary Bessel functions of the first kind of order 0 and 1, respectively
L = distance between the circular plates, m
P = dimensionless pressure
ΔP_E = dimensionless total excess pressure drop
$P(\rho), S(\xi, \rho), W(\xi, \rho)$ = functions introduced in Eqs. 5, 6, and 7
Q = total flow rate, m^3/s (or dimensionless)
R = radius of the pipe, m
u = dimensionless axial velocity
v = dimensionless radial velocity

Greek letters

α_n, β_n = zeros of J_0 and J_1, respectively
β, ρ = integration variables
$\eta, \hat{\eta}$ = dimensionless axial coordinate z/R, z/L
κ = aspect ratio L/R
μ = fluid viscosity, kg/m/s
ξ = dimensionless radial coordinate r/R
ψ = dimensionless stream function
ω = dimensionless vorticity

Superscripts, subscripts, and special symbols

k, n = kth, nth term in an infinite series expansion
$*, \wedge$ = quantities pertaining to the plane $z=0$, the region $z>0$

Literature Cited

Bird, R. B., W. E. Stewart, and E. N. Lightfoot, *Transport Phenomena*, Wiley, New York (1960).

Chatterjee, A., and D. White, "Radial Entry Flow of a Newtonian Fluid," *J. Phys. D: Appl. Phys.*, **22**, 915 (1989).

Chen, C.-P., "Contribution a l'Etude Expérimentale de l'Écoulement Radial d'un Fluide Visquex Incompressible Entre Deux Disques Parallèles," *J. Mec.*, **5**, 245 (1966).

Dagan, Z., S. Weinbaum, and R. Pfeffer, "An Infinite Series Solution for the Creeping Motion through an Orifice of Finite Length," *J. Fluid Mech.*, **115**, 505 (1982).

Hollahan, J. R., and R. S. Rosler, "Plasma Deposition of Inorganic Thin Films," *Thin Film Processes*, J. L. Vossen and W. Kern, eds., Academic Press, New York (1978).

Hunt, J. B., and I. Torbe, "Characteristics of a Hydrostatic Thrust Bearing," *Int. J. Mech. Sci.*, **4**, 503 (1962).

IMSL, *International Mathematical and Statistical Library of Subroutines*, IMSL Inc., Houston (1989).

Jackson, J. D., and G. R. Symmons, "The Pressure Distribution in a Hydrostatic Thrust Bearing," *Int. J. Mech. Sci.*, **7**, 239 (1965a).

Jackson, J. D., and G. R. Symmons, "An Investigation of Laminar Radial Flow Between Two Parallel Discs," *Appl. Sci. Res.*, **15**, 59 (1965b).

Livesey, J. L., "Inertia Effects in Viscous Flows," *Int. J. Mech. Sci.*, **1**, 84 (1960).

Middleman, S., *Fundamentals of Polymer Processing*, McGraw Hill, New York (1977).

Moller, P. S., "Radial Flow without Swirl Between Parallel Discs," *Aeronaut. Quart.*, **14**, 163 (1963).

Parmet, I. L., and E. Saibel, "The Flow of Perfect and Viscous Fluids in a Radial Diffuser," *Zeit. Angew. Math. Mech.*, **45**, 409 (1965).

Peube, J.-L., "Sur l'Écoulement Radial Permanent d'un Fluide Visquex Incompressible Entre Deux Plans Parallèles Fixes," *J. Mec.*, **2**, 377 (1963).

Sampson, R. A., "On Stokes' Current Function," *Phil. Trans. R. Soc. Lond.*, **A182**, 449 (1891).

Shanks, D., "Nonlinear Transformations of Divergent and Slowly Convergent Sequences," *J. Math. Phys.*, **34**, 1 (1955).

Takematsu, M., "Slow Viscous Flow Past a Cavity," *J. Phys. Soc. Japan*, **21**, 1816 (1966).

Vrentas, J. S., and J. L. Duda, "Effect of Axial Diffusion of Vorticity on Flow Development in Circular Conduits: II. Analytical Solution for Low Reynolds Numbers," *AIChE J.*, **13**, 97 (1967).

Manuscript received Dec. 28, 1992, and revision received Feb. 4, 1993.